PNAS

www.pnas.org

Supplementary Information for

Biocompatible surface functionalization architecture for a diamond quantum sensor

Mouzhe Xie^1, Xiaofei Yu^2, Lila V. H. Rodgers[3], Daohong Xu[2], Ignacio Chi-Durán[4], Adrien Toros[5], Niels Quack[6], Nathalie P. de Leon[3], Peter C. Maurer*[1]

[1] Pritzker School of Molecular Engineering, the University of Chicago, Chicago, IL 60637, USA

[2] Department of Physics, the University of Chicago, Chicago, IL 60637, USA

[3] Department of Electrical and Computer Engineering, Princeton University, Princeton, NJ 08544, USA

[4] Department of Chemistry, the University of Chicago, Chicago, IL 60637, USA

[5] Center of MicroNanoTechnology, École polytechnique fédérale de Lausanne, Lausanne, CH-1015, Switzerland

[6] Institute of Microengineering, École polytechnique fédérale de Lausanne, Lausanne, CH-1015, Switzerland

^ Equal contribution

* Peter C. Maurer
Email: pmaurer@uchicago.edu

This PDF file includes:

Supplementary Tables and Figures:
- Tables S1 to S3
- Figures S1 to S19

Captions for Supplementary Movies S1 and S2
SI References

Supplementary Tables and Figures:

Supplementary Table S1. The key parameters, including the estimated layer thickness (d_E, D_S, D_E, and D_{Max}) using different methods, of PEG molecules used in this study.*

|	Number of units	d_E (nm)	D_S (nm)	D_E (nm)	D_{Max} (nm)
PEG$_8$	8	0.99	0.89	0.85	1.00
PEG$_9$	9	1.05	0.92	0.89	1.06
PEG-2000 Da	45	2.35	2.21	2.11	2.53
PEG-3400 Da	77	3.07	2.88	2.77	3.36
PEG-5000 Da	114	3.73	3.54	3.45	4.14

* d_E (nm) is the end-to-end distance assuming Gaussian chain behavior in a good solvent, while D_S, D_E, and D_{Max} are metrics from analyzing 1000 simulated surface-anchored chains. See Figure S4 caption for detail.

Supplementary Table S2. Final fitting parameters of the curves in Figure 4D using Eqs. [1] and [2] in the main text.

	$T_2(1)$ (µs)	s	N_{sat}
NV No. 2 Bare	7.04	0.40	-
NV No. 2 Functionalized	0.70	0.64	-
NV No. 7 Bare	23.70	0.44	130.082
NV No. 7 Functionalized	28.01	0.25	-

Supplementary Table S3. Final fitting parameters of the curves in Supplementary Figure S18 using Eq. [2] in the main text.

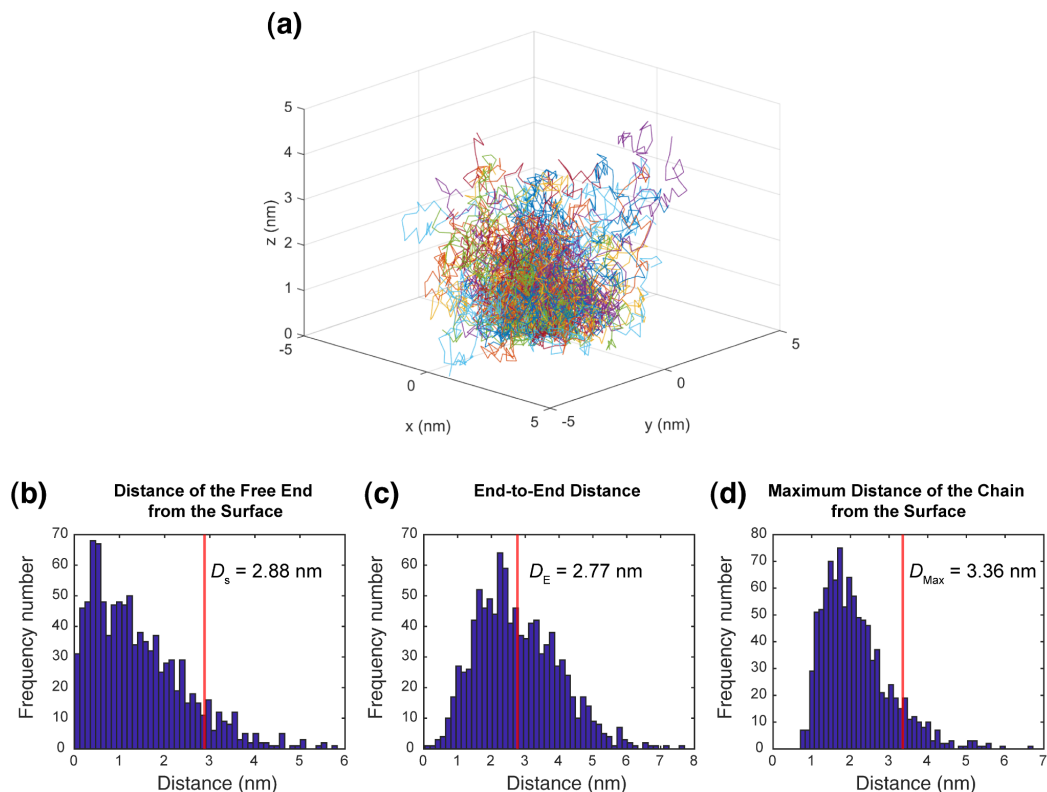|	$T_2(1)$ (µs)	s
Bare in oil	14.82	0.31
Bare in water	5.19	0.14
Functionalized in oil	1.91	0.47
Functionalized in water	2.57	0.36
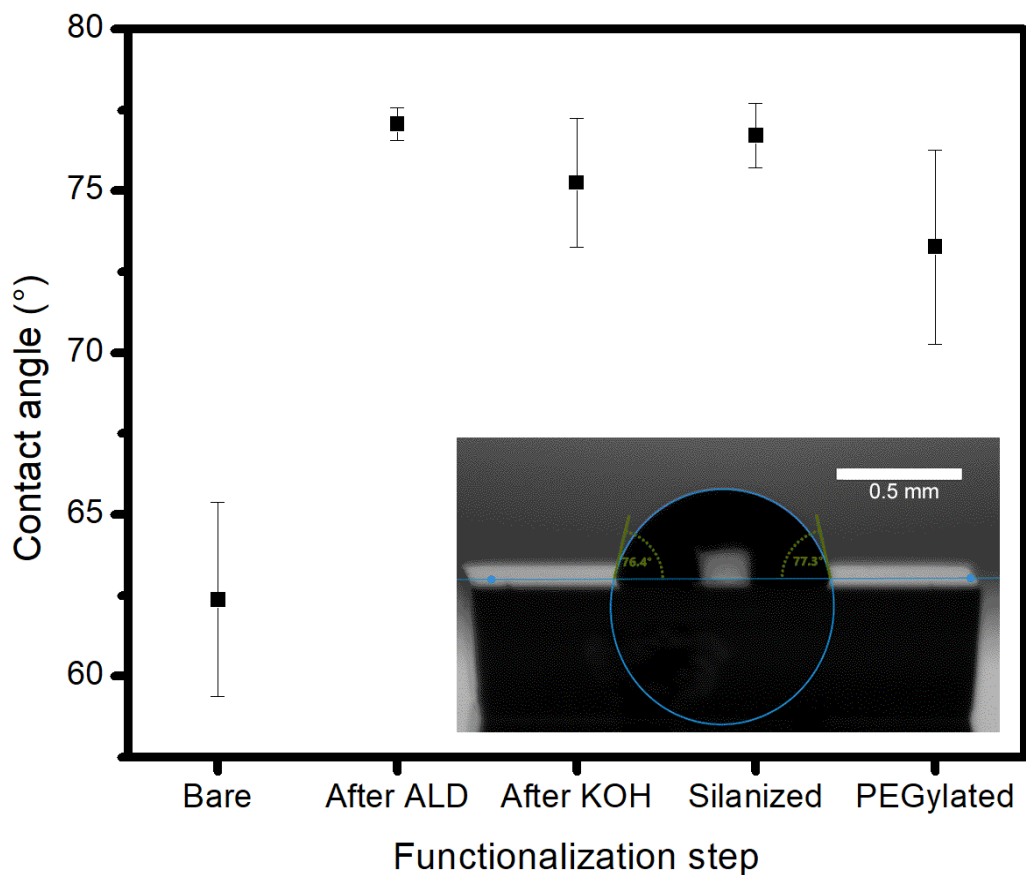
Supplementary Figure S1. Water contact angle measurement at different stages of diamond surface functionalization. Contact angle measurements were performed with a Drop Analyzer Surface KRUSS DSA100 using a drop volume of 0.2 µL DI water. The contact angle was calculated based on the fitted curvature of each drop using the ellipse model in ADVANCE software. Prior to the measurements, diamond samples were rinsed with DI water, dried with N_2 gas flux, and then placed in an oven at 60°C for one hour. Error bars represent standard deviation from four repeated measurements. Sample was water-rinsed and oven-dried between measurements. Inset: drop shape on a PEGylated diamond surface with the ellipse model used to extract the contact angle.
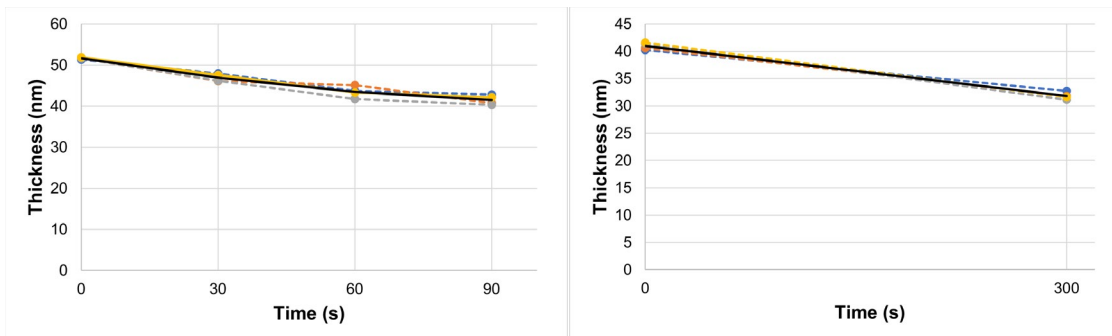
Supplementary Figure S2. Measured dissolution rate of Al_2O_3 in KOH solutions. An 38nm thick Al_2O_3 film deposited with ALD on a diamond sample was patterned with a Heidelberg Direct Write Lithography system (AZ MiR 703 photoresist spin-coated 1 µm and developed for 1 min in AZ 300MIF) and back etched (Cl_2/Ar in a Plasma-Therm ICP Etch system at 400 W ICP power for 55 s). A resulting diamond samples with lithographically patterned Al_2O_3 structures were submerged in (left) 1 M and (right) 10 mM KOH for a fixed duration, rinsed immediately with water, and dried with N_2 gas. The AFM measurements were done on the same features at four distinct locations (colored circles and dashed lines). The mean values are indicated by the black solid lines. The dissolution rates are determined as 3.6 nm/min and 1.8 nm/min, respectively.

(a)

(b)
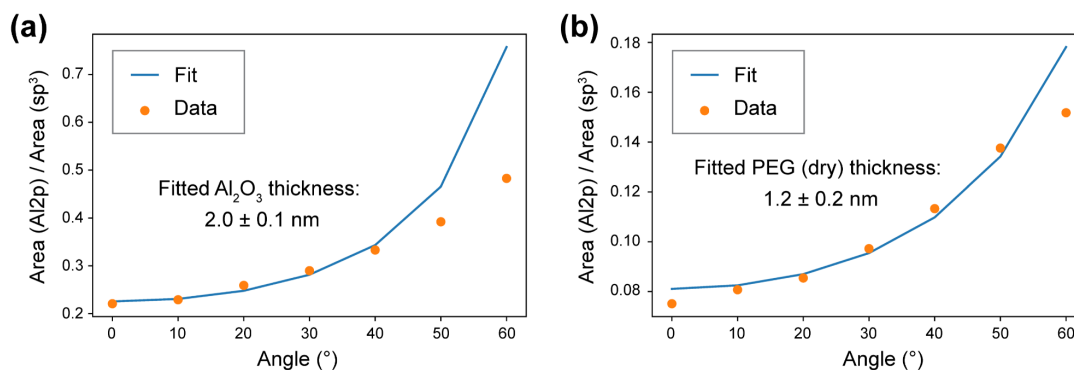
Supplementary Figure S3. Estimation of Al_2O_3 and PEG thicknesses by ARXPS. XPS was conducted using a Thermo Fisher K-Alpha and X-ray Spectrometer Tool with an Al K-alpha source (1486 eV) at Princeton University in the Imaging and Analysis center. Data were collected using a 250 μm spot size and a flood gun to mitigate charging. For the estimation of the thickness of the Al_2O_3 and PEG layers, the angle between sample and detector was varied from 0-60° using angle-resolved XPS (ARXPS). Only 0° to 40° data were used for the fittings. The fitted results nicely follow the data except for at the higher angles, possibly owing to the pronounced elastic scattering under those conditions. Attenuation length values for photoelectrons passing through the different materials were taken from the NIST database. **(a)** A diamond sample was deposited with 2 nm Al_2O_3 by thermal ALD (20 cycles of TMA + H_2O at 200°C). A 2-layer model (Al2p: only from Al_2O_3; C-sp^3: only from diamond) as described in Ref. ([1](#)) was used to fit and extract the Al_2O_3 layer thickness. A density of 3.25 g/cm^3 was used for amorphous Al_2O_3. The fitted thickness is 2.0 ± 0.1 nm, which is in agreement with the expected value. **(b)** A diamond sample with 2 nm Al_2O_3 was silanized and PEGylated (using mPEG-2000 Da) following the standard protocol introduced in this study. A 3-layer model (Al2p: only from Al_2O_3; C-sp^3: from both diamond and PEG layer) was used to fit and extract the PEG layer thickness. We only achieved reasonable fitting when the thickness of the intermediate Al_2O_3 layer was fixed to 1.0 nm, which is attributed to imperfections of the model. A PEG density of 0.3 g/cm^3 was assumed, which was estimated from the volume occupied by each surface-bound PEG molecule (see the simulation in [Fig. S4](#)). The PEG layer thickness is determined to be 1.2 ± 0.2 nm. Note that the ARXPS data was collected under ultrahigh vacuum and the PEG molecules may have collapsed. Errors for both thickness estimates are standard errors from the fits. The PEG layer thickness was also estimated by other methods, see [Table S1](#) and [Figure S4](#) for detail.

(a)

(b) Distance of the Free End from the Surface

D_s = 2.88 nm

(c) End-to-End Distance

D_E = 2.77 nm

(d) Maximum Distance of the Chain from the Surface

D_{Max} = 3.36 nm

Supplementary Figure S4. Statistical analysis of 1000 simulated 3-dimensional random coil chains. PEG molecule can be modeled as a random coil chain comprising N ethylene units with ethylene unit length of a. The reported value of a is between 0.27 - 0.42 nm under different assumptions and conditions (2-5). We use a = 0.35 nm in our simulation. N can be calculated from the average molecular weight, M, by $N = M / 44$. Chains were generated in MatLab from the (0, 0, 0) origin with N number of connecting vectors, each of which has a fixed length of a and randomly oriented in a 3-dimensional space. No part of the chains is allowed to have negative z value, namely the chains are above the "surface" (x-y plane). **(a)** In this example, N = 77 (equivalent to average m.w. 3400) and a = 0.35 nm. Only 200 chains are displayed. **(b)** Histogram of the distance of the free end from the surface. Red vertical line indicates the 90 percentile, denoted D_S. **(c)** Histogram of the distance of the free end from the origin, namely end-to-end distance. Red vertical line indicates the mean value, denoted D_E. **(d)** Histogram of the maximum distance of any part of each chain from the surface. Red vertical line indicates the 90 percentile, denoted D_{Max}. In addition, we also estimated the PEG layer thickness based on the end-to-end distance d_E of a single PEG molecule, assuming a Gaussian chain behavior in a good solvent, namely $d_E = a\sqrt{N}$. The estimated thicknesses of all PEG molecules used in this study based on the above-mentioned methods are summarizes in Table S1. In addition, we determined the vacuum-dried thickness of mPEG-2000 Da to be 1.2 ± 0.2 nm based on angle-resolved X-ray photoelectron spectroscopy (ARXPS) data at various incidence angles, ranging from 0° to 60°. See Figure S3 and the caption for detail.

mPEG   0.04%   0.2%   1% biotinPEG
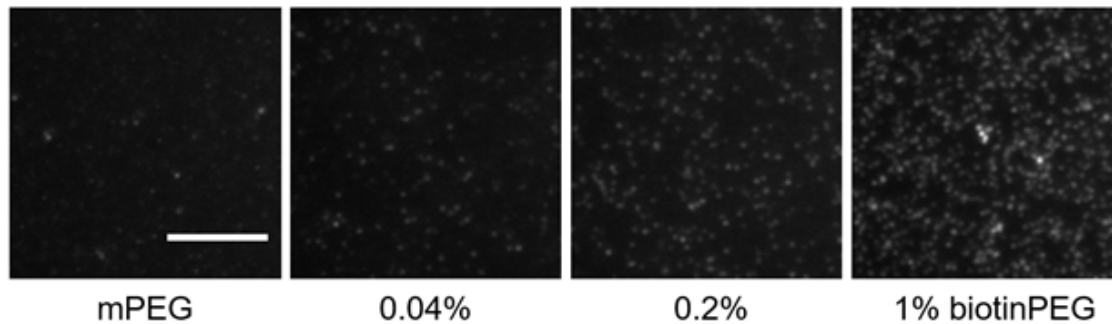
Supplementary Figure S5. Single-molecule fluorescence images showing the controllable functionalization using shorter PEG. Surfaces were functionalized with $mPEG_8$ and $biotinPEG_9$, leading to a PEG thickness of approximately 1 nm (see Table S1). Thus, the overall thickness of the functionalization architecture achieved here is roughly 3 nm (2 nm Al_2O_3 + 1 nm PEG). Imaged in Antifade medium. Scale bar 5 μm.

1.5 nM   **7 nM**   **35 nM**
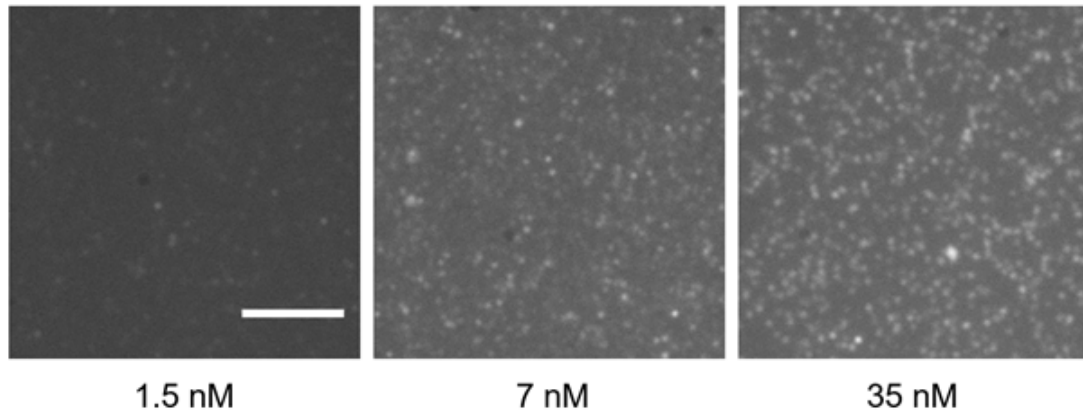
Supplementary Figure S6. Dependence of grafting density on protein concentration. The diamond surfaces were all functionalized with 1% biotinPEG, yet incubated with Alexa-488 labeled streptavidin solution at various concentrations. As expected, the more concentrated solution leads to larger grafting density. Scale bar 5 μm.
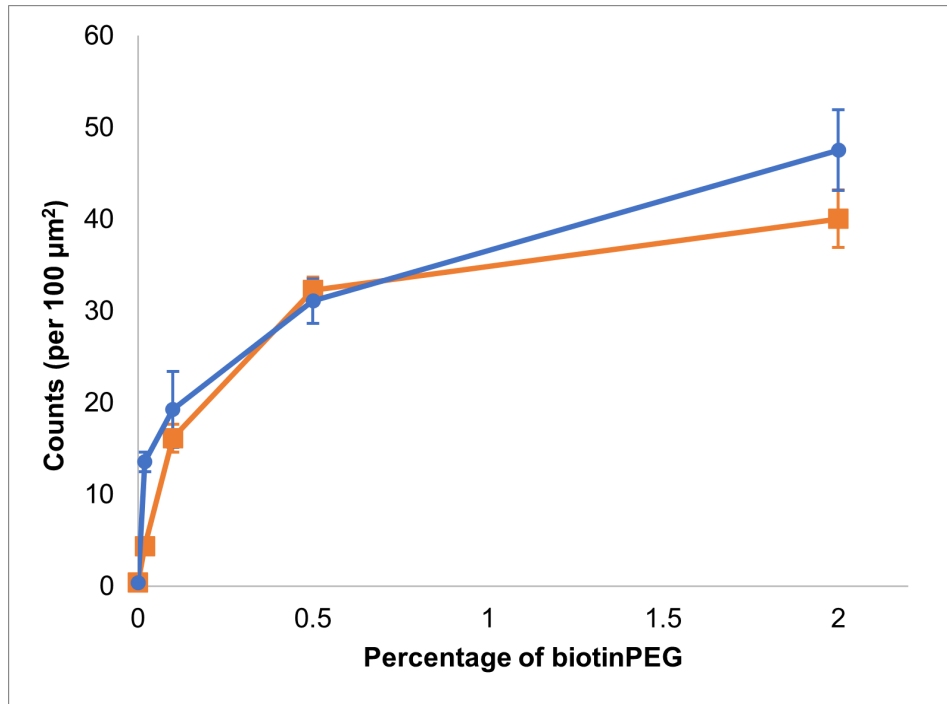
Supplementary Figure S7. Quantitative analysis of the grafting density of Alexa-488 labeled SA on diamond surfaces as a function of biotinPEG percentage. Two independent experiments (blue and orange lines) were conducted, suggesting good reproducibility. Error bars are the standard deviation of the grafting density calculated based on three images (each has a field-of-view of approximately 2800 μm^2) for each data point. Representative images are shown in main text Figure 2*A*. Note that at higher densities, individual fluorophores were no longer spatially resolved during image analysis.
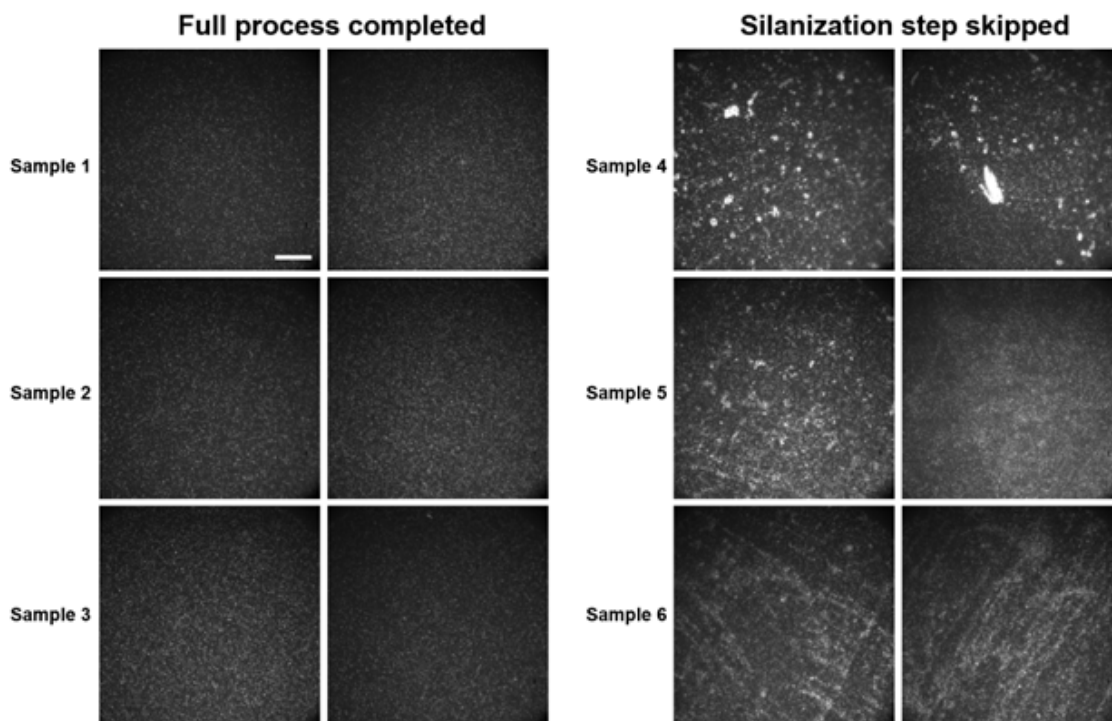
Supplementary Figure S8. Single-molecule fluorescence images of Alexa-488 labeled streptavidin immobilized to diamond surfaces. The left column displays representative images of 3 diamond samples (2 images each) that completed all the functionalization steps, which show remarkable homogeneity of the spatial distribution of immobilized streptavidin molecules. By contrast, the right column displays selected images (not necessarily representative) of 3 diamond samples that were identically prepared in the same batch except for skipping the silanization step, where various forms of inhomogeneity can be seen. Clearly, the silanization step is critical to achieve uniform and reproducible functionalization. Al_2O_3 layers of 50 nm thickness were used here. Samples were imaged in the sodium phosphate buffer. Scale bar 10 μm.
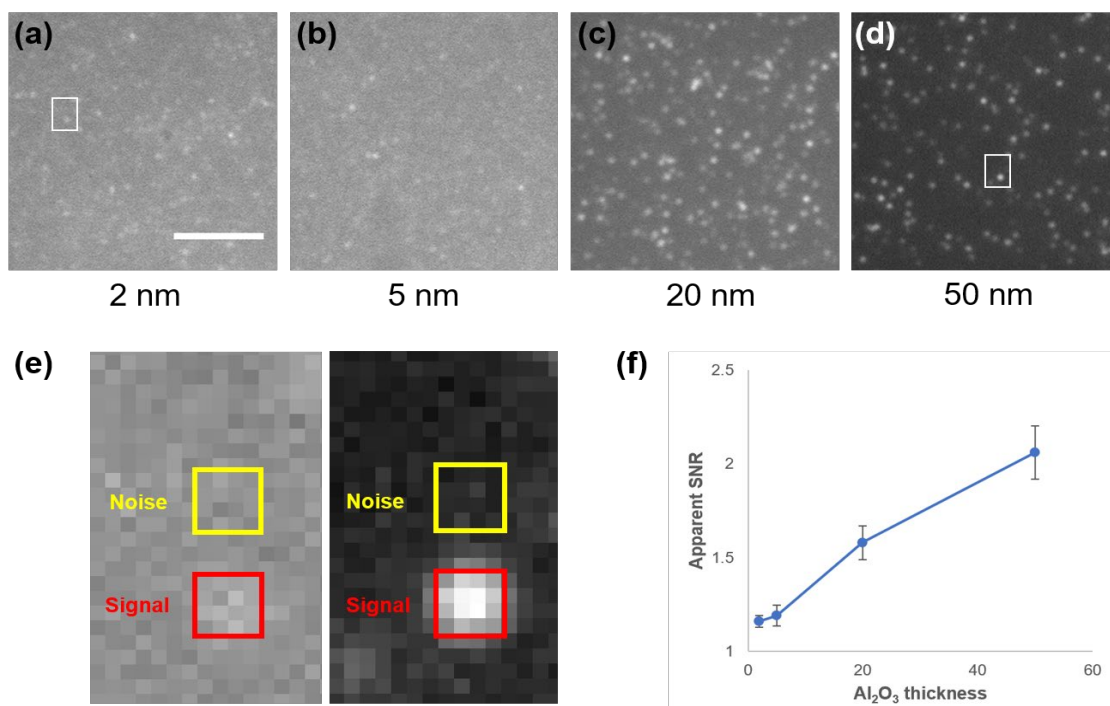
Supplementary Figure S9. The apparent signal-to-noise ratio (SNR) of fluorescence images in response to different Al_2O_3 layer thickness. **(a-d)** Representative single-molecule fluorescence images with epi-fluorescence illumination of Alexa-488 labeled streptavidin immobilized to diamond surfaces with varying Al_2O_3 thickness in sodium phosphate buffer. A clear reduction of the fluorophore SNR can be observed as the Al_2O_3 layer thickness goes thinner. Scale bar 5 μm. **(e)** Zoom-in of the boxed regions in (a) and (d). We define the sum of intensities of a 4×4-pixel area over a fluorescent spot (red boxes) as the "signal" and the sum of intensities of a 4×4-pixel area over a nearby background region (yellow boxes) as the "noise", from which SNR was calculated. **(f)** The mean of apparent SNR quantified using the method introduced in (e), based on 10 clearly distinguishable fluorescent spots in each image. Error bars denote one standard deviation.
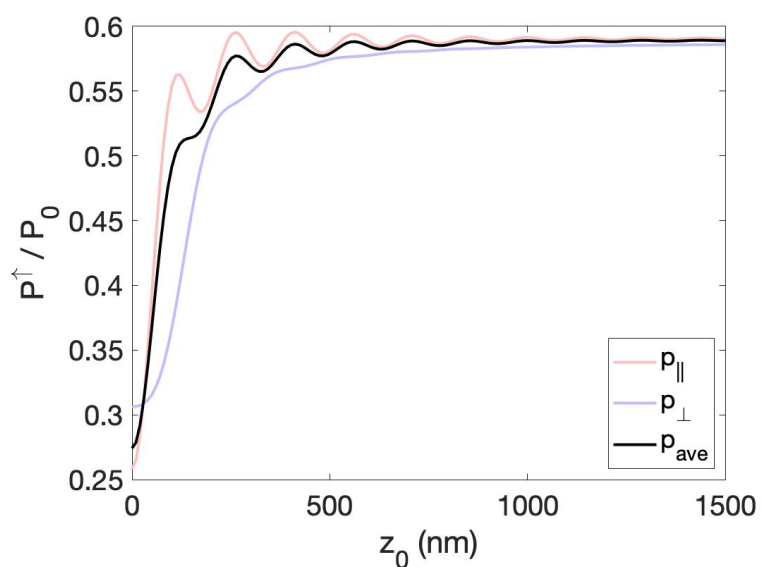
Supplementary Figure S10. compares the optical power emitted away from the diamond surface ($P_\uparrow$) to the total power radiated (P_0) into all directions, including surface guiding modes. The calculations are based on an analytical solution ([6](#)) for a dipole separated a distance (z_0) from a diamond-Al_2O_3 interface. The red line indicates the emitted power for a dipole parallel to the diamond surface, while the blue line denotes a dipole perpendicular to the surface. The black line shows the emitted power for an isotropic molecule orientation. The fluorophore emission spectrum is extracted from https://www.fpbase.org/spectra/.
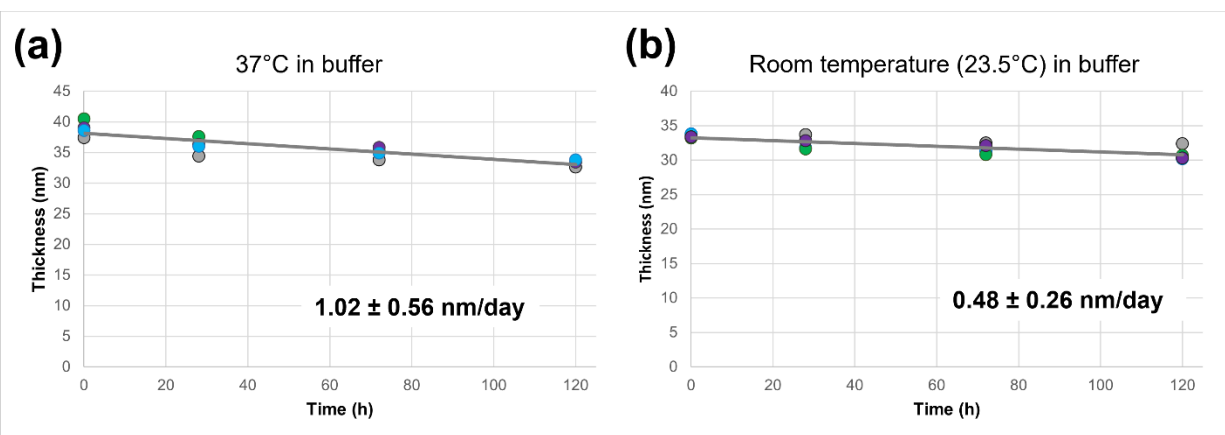
Because of this, for single-molecule imaging experiments on samples that were coated with thin Al_2O_3 layers, Invitrogen SlowFade Diamond Antifade Mountant (refractive index 1.42) was used to improve SNR.
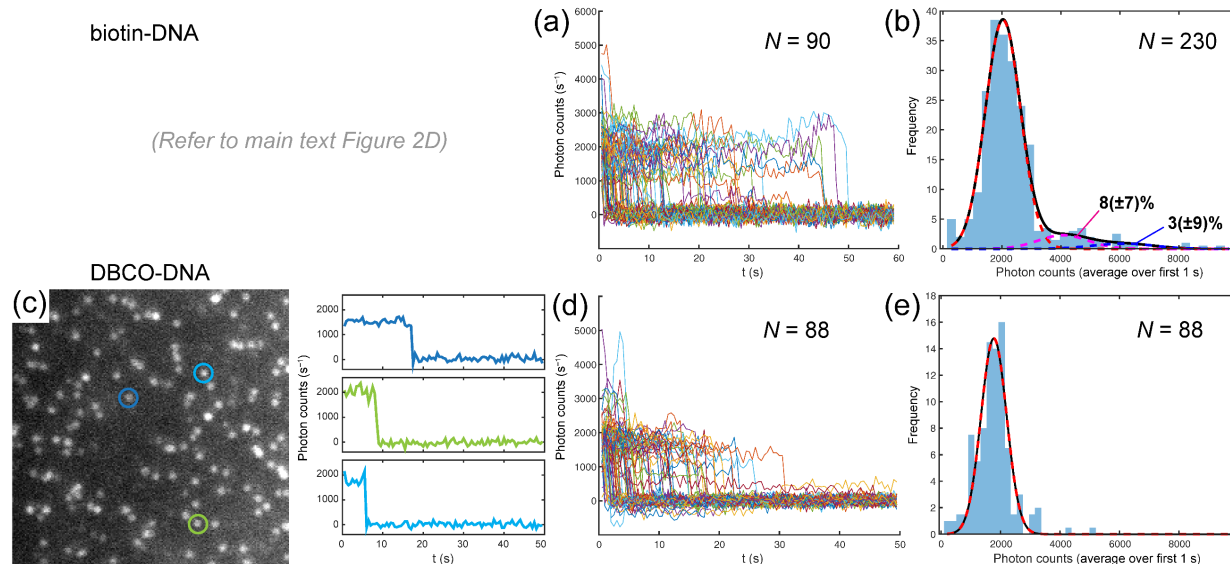
Supplementary Figure S11. Selected time traces of the Cy3 dye on the ssDNA immobilized to diamond surfaces via (top) a biotin tag and (bottom) a 5'- DBCO tag, imaged in Antifade medium. In a typical experiment, we recorded a movie comprising 500 ms × 100 (or 120) frames of images that have 512 × 512 pixels. Each movie was converted to a 16-bit TIF file. Based on the 1st frame, individual fluorescence spots were identified using ImageJ by setting appropriate intensity cut-off and their rough positions were saved as a peak list. For each fluorescent spot, a 9 × 9-pixel square was created around its rough position, and a Gaussian fit was performed (only on the 1st frame) to find out the accurate position as well as the standard deviation s. To extract intensity from each frame, we sum up the data values of all the pixels in a squared regions with edge length of s (typically 3 or 4 pixels) centered at the identified accurate position, subtracting the normalized background intensity defined by the residual region in the 9 × 9-pixel square. The final intensity has been accounted for file conversion and is reported as photon counts per second (s^{-1}). We typically only analyze the center 256 × 256-pixel region of each movie, and fluorescence spots that were not completely photon-bleached by the end were eliminated for subsequent ensemble analysis. **(a)** In total 90 fluorescence intensity traces extracted from a 256 × 256-pixel region of main text Figure 2D and plotted in the same figure. Most of the traces have similar plateau values around 2000 counts/s and several traces display two-step decay behavior, as shown in Figure 2D. **(b)** Histogram of the average intensities over the first second (first 2 frames) from in total 230 traces based on three movies, decomposed to three Gaussian distributions that have equally spaced centers and same standard deviation. This allows us to estimate the population of biotin-DNA : nSA = [1:1, 2:1, and 3:1] complexes to be [89%, 8(±7)%, and 3(±9)%], respectively (the "±" uncertainties are based on 95% confidence interval from the fit and only reported for small percentages). **(c)** A single-molecule fluorescence image (200 × 200-pixel area) of Cy3 dye on ssDNA immobilized via SPAAC, together with three representative time traces. **(d)** We were able to extract in total 88 traces and plotted in the same figure. **(e)** Histogram of the average intensities over the first second (first 2 frames) of these 88 traces fitted to a single Gaussian distribution.

13
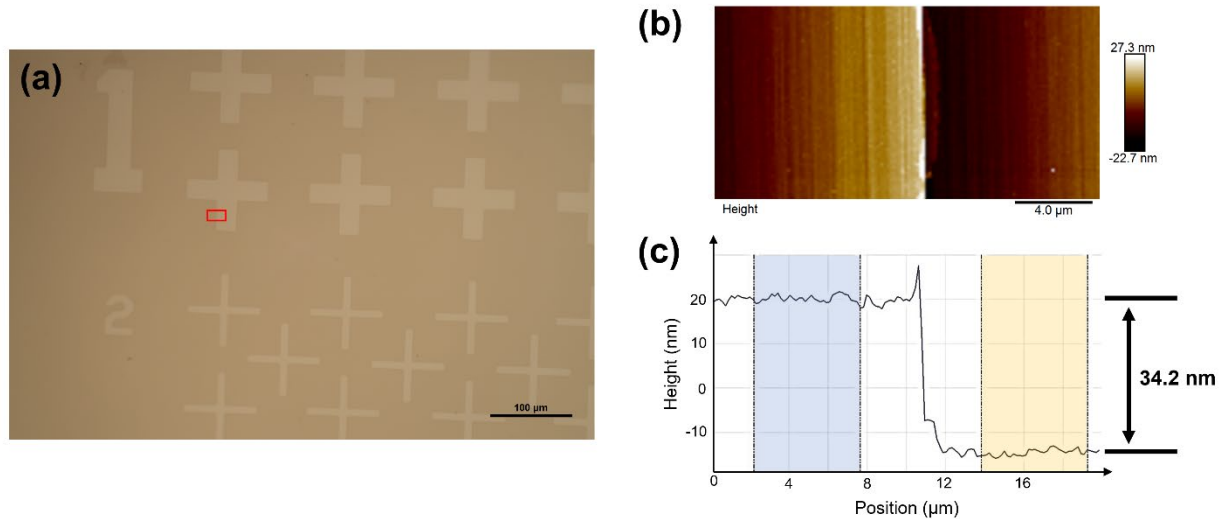
Supplementary Figure S12. Examples of measuring the remaining thickness of the functional layer. **(a)** Optical image of a diamond chip with lithographically patterned Al_2O_3 layer that was also silanized and PEGylated using the protocol described in the current study. Cross-shapes are where Al_2O_3 had been removed by reactive ion etch. **(b)** AFM scan (20×10 μm^2, 128×64 lines) of the region indicated by a red box in (a) (roughly drew by hand). AFM was performed on a Bruker Dimension Icon instrument with SCANASYST-AIR tips. The image has been flattened to the 1st order using NanoScope Analysis software. **(c)** The 2D profile of (b) averaged along the short edge. The profile has been leveled (1st order) to correct the baseline. The height difference can thereafter be extracted based on the two color-shaded regions, which reflects the thickness of the remaining functional layer in respect to diamond substrate.
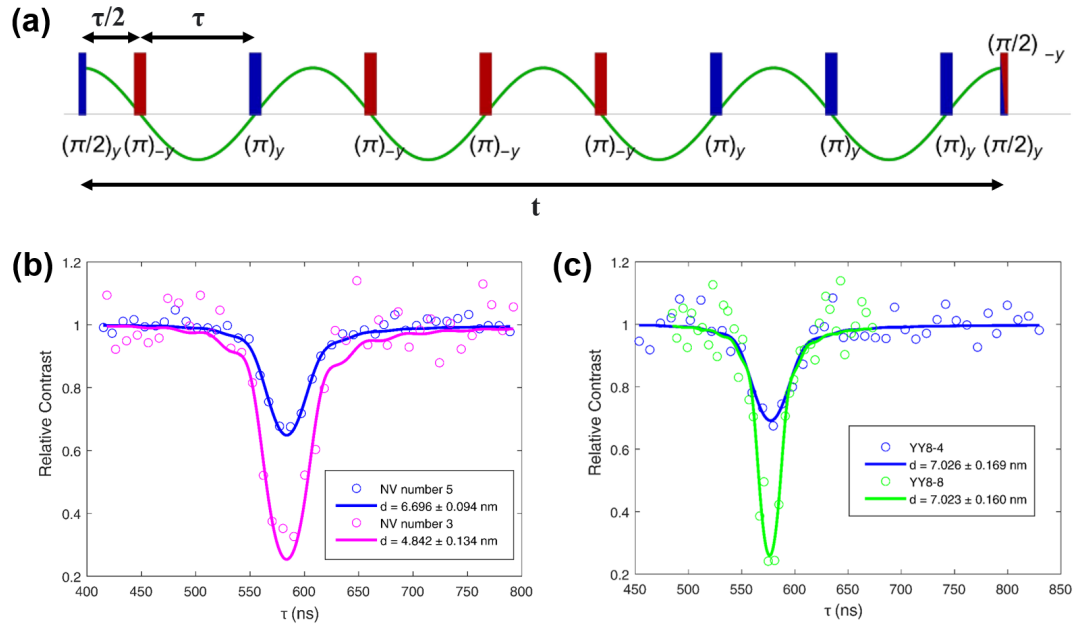
(a) 37°C in buffer

Thickness (nm) vs Time (h)

1.02 ± 0.56 nm/day

(b) Room temperature (23.5°C) in buffer

Thickness (nm) vs Time (h)

0.48 ± 0.26 nm/day

Supplementary Figure S13. Dissolution rate measured at **(a)** 37°C and **(b)** 23.5°C in buffer (pH 7.4, [NaH$_2$PO$_4$ + Na$_2$HPO$_4$] = 50 mM, [NaCl] = 100 mM). The uncertainty (±) reflects 95% confidence interval from fitting the averages.

| 0 h | 24 h | 96 h |
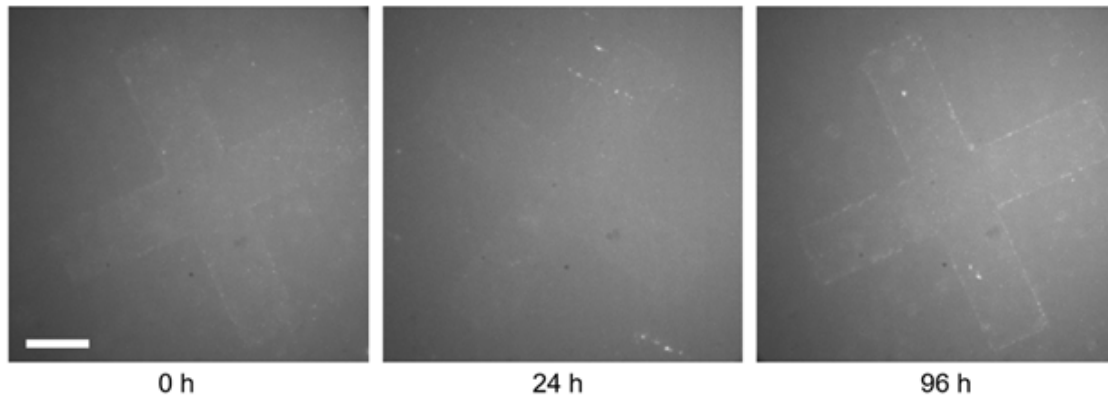
Supplementary Figure S14. Fluorescence images of "cross" shaped Al_2O_3 patterns (2 nm thickness) lithographically written on a diamond sample, which was immersed in 50 mM pH 7.4 sodium phosphate buffer (also contained 100 mM NaCl) at room temperature, over a course of 4 days. The pattern was created by a lift-off (for 2 nm thin layer) process. Specifically, diamond was patterned with AZ MiR 703 photoresist on a Heidelberg Direct Write Lithography system with 375 nm laser exposure, then deposited with 2 nm thick Al_2O_3 (20 cycle, 200°C, the photoresist color turned red at this temperature, but patterns were unperturbed), and finally lifted off in 80°C NMP for 40 min under sonication.

In these optical images (488 nm laser excitation), the Al_2O_3 regions are slightly brighter, possibly due to the presence of fluorescent crystal defects in the ALD Al_2O_3. Such contrast disappeared rapidly during short exposure (~5 s) to the ~30 mW 488 nm excitation laser, making the attempt to directly compare the remaining thickness (deduced from the contrast) between images almost impossible. Certain patterns (especially the rightmost one) exhibit extraordinarily bright edges, which likely originate from remaining photoresist due to incomplete lift-off during lithography as shown in main text Figure 1*F* by AFM. Importantly, no visible damages, including pinholes or pill-off of edges, to these patterns were observed during the entire period, suggesting that the Al_2O_3 thin layer is stable under (near-)physiological conditions. Scale bar 10 µm.

(a) $\tau/2$ $\quad\tau$

$(\pi/2)_y\ (\pi)_{-y}\quad(\pi)_y\quad(\pi)_{-y}\quad(\pi)_{-y}\quad(\pi)_{-y}\quad(\pi)_y\quad(\pi)_y\quad(\pi)_y\ (\pi/2)_y$ $\quad(\pi/2)_{-y}$

t

**Supplementary Figure S15.** YY8 pulse sequence and the robustness of our NV depth measurement.
(a) An illustration of the YY8 pulse sequence. Eight π-pulses with either y or $-y$ phase equally spaced by time τ are placed between two $\pi/2$-pulses. The last $\pi/2$-pulse has a 180° phase shift to cancel out common mode noise. The entire duration of the YY8 pulse is denoted by t, which is the x-value in the main text Figure 4*B*. We used YY8 pulse sequences, which, compared to commonly used XY-type sequences, can effectively avoid the higher-order spurious signal due to pulse imperfection ([7]). **(b)** Examples of the depth measurement. Two NV centers of different depths give rise to clearly different relative contrast. **(c)** Depth measurement on the same NV center using different number of π-pulses returns essentially the same results, which verify the robustness of the method. All measurements were performed at 200 G, which results in a Larmor precision frequency that conveniently accessible by our XY-lock-in measurement technique.

17
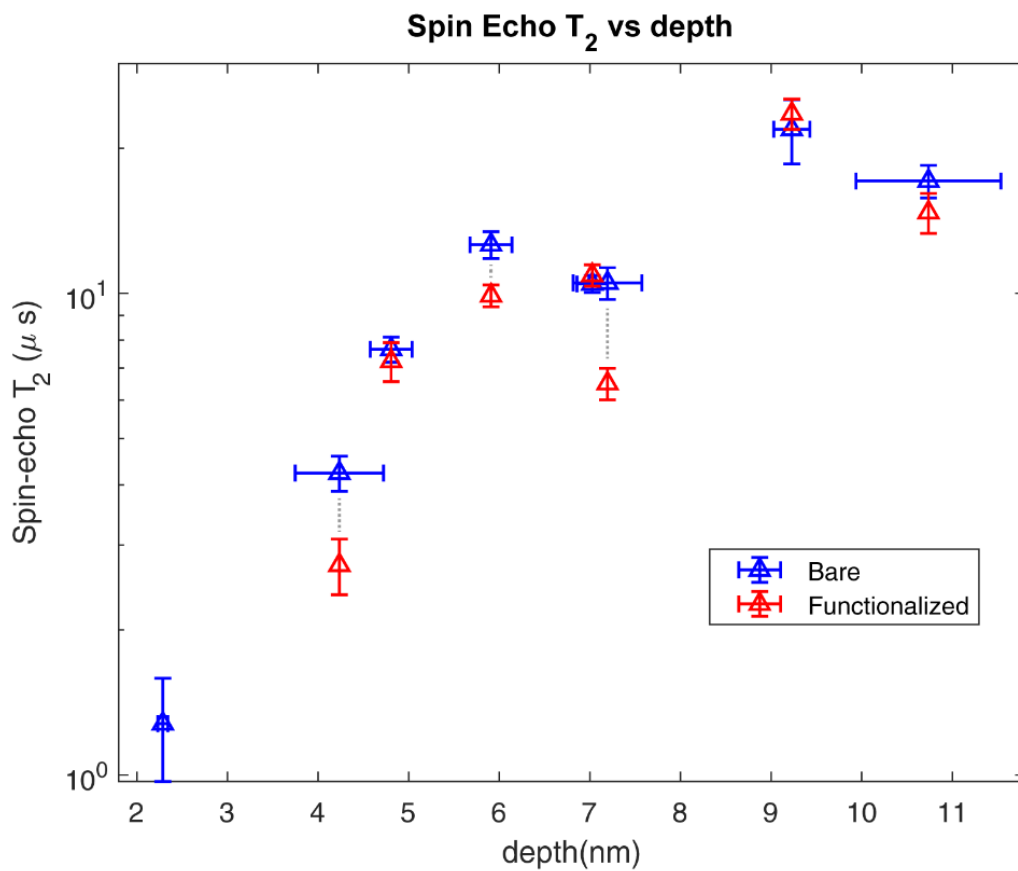
Supplementary Figure S16. T_2 measured by spin-echo pulse sequence plotted against NV depth before (blue) and after (red) functionalization for the same set of NV centers shown in the main text Figure 4. Analogous to the YY8 pulse in main text Figure 4*C*, a typical T_2 dependence on NV depth is seen. The fold-decreases in T_2 after functionalization measured by spin-echo is, however, much smaller than the ones revealed by YY8 sequences.
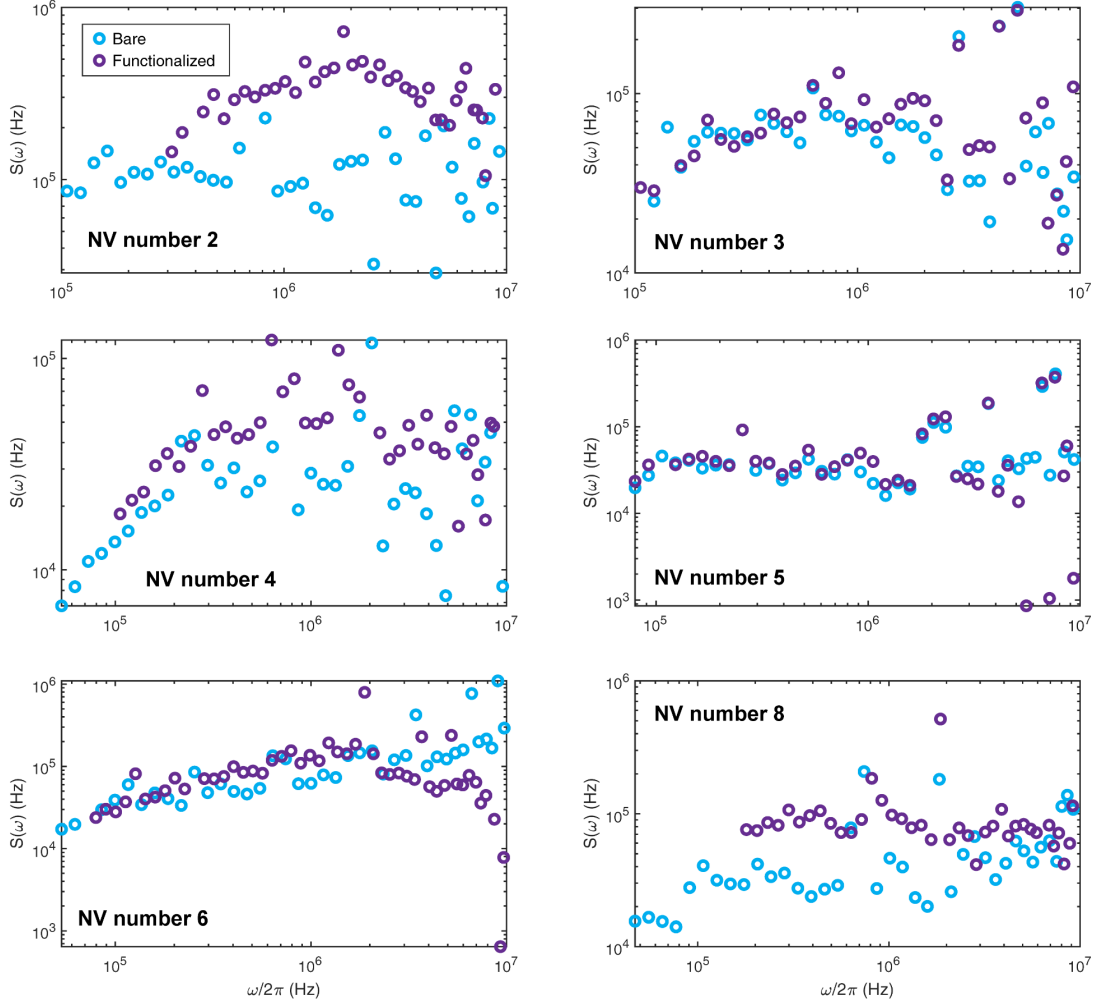
Supplementary Figure S17. Additional noise spectra for NV centers, same as the one shown in the main text Figure 4*E*. Spectral decomposition manifests a broadband noise spectrum across the frequency range of 0.05-10 Mhz. The spectral density of noise $S(\omega)$ can be estimated from coherence measured by dynamical decoupling sequence ([8-10](#)). The measurement contrast can be written as $C(t) = e^{-\chi(t)}$ (with $\chi(t) = \frac{1}{\pi}\int \frac{S(\omega)}{\omega^2} 8\sin^4(\frac{\omega t}{4N})\frac{\sin^2(\frac{\omega t}{2})}{\cos^2(\frac{\omega t}{2N})}d\omega$ (note, *N* refers to the number of π-pulses)). For large *N*, where $F_N(\omega t)$ is sharply peaked at $\omega = \pi N/t$, Eq. S2 can be approximated as $\chi(t) \approx \frac{tS(\omega)}{\pi}$.
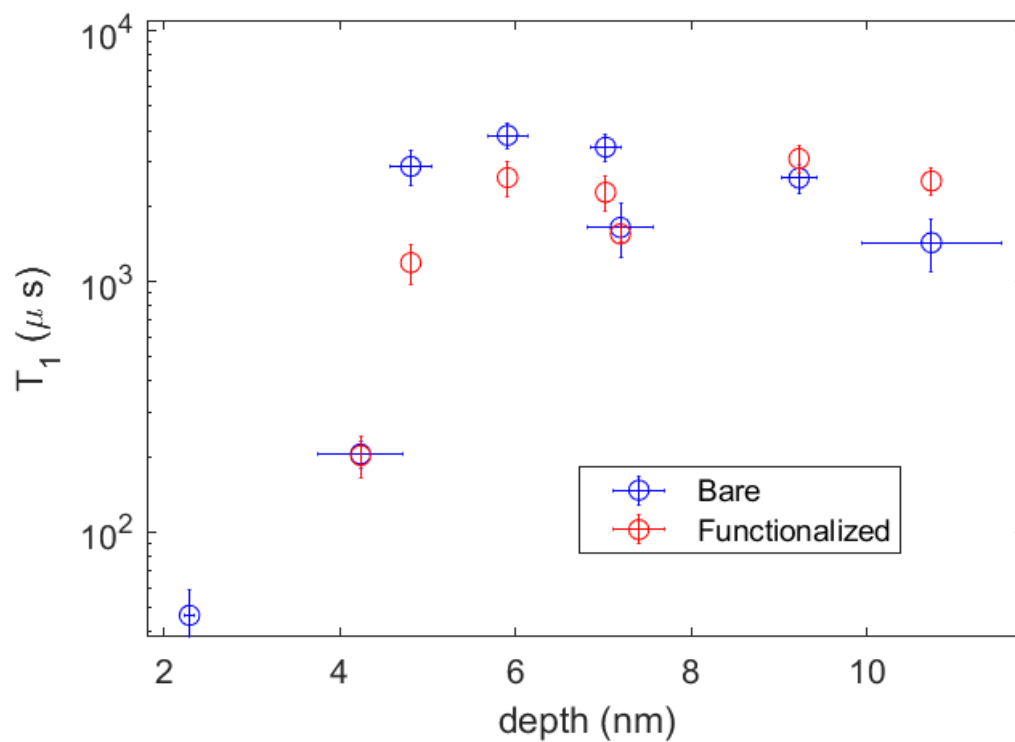
Supplementary Figure S18. T_1 plotted against depth before (blue) and after (red) functionalization for the same set of NV centers shown in the main text Figure 4.
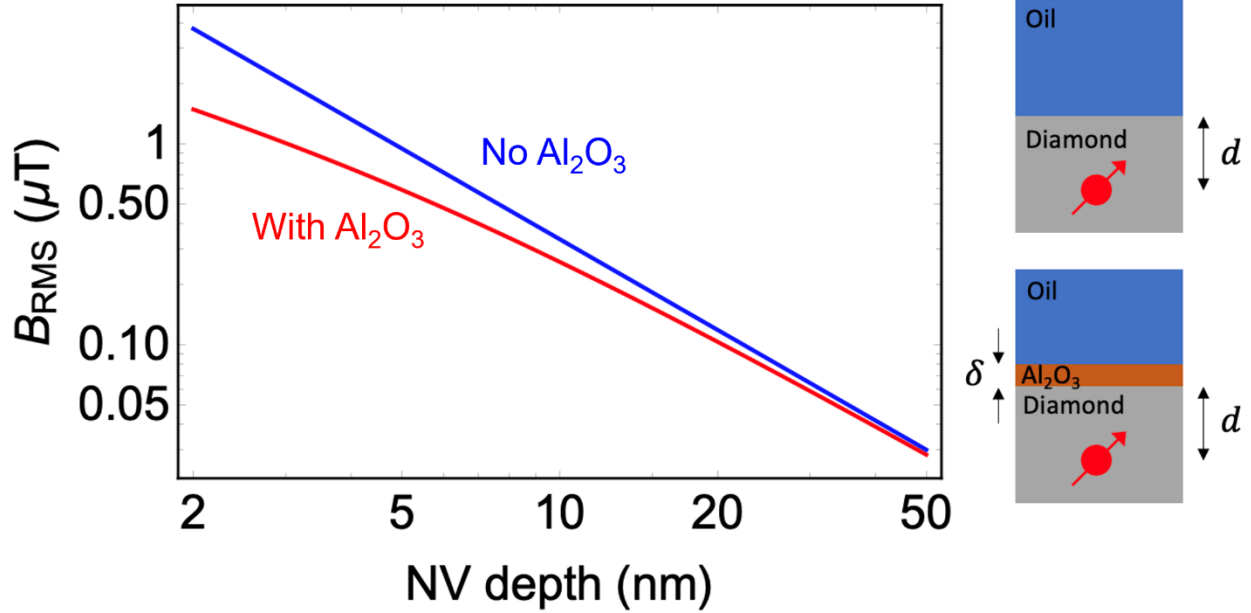
Supplementary Figure S19. The graph shows analytical results for the root-mean-square magnetic field noise (B_{rms}) that is experienced by an NV center of depth (d) below the diamond surface. The blue curve corresponds to a bare diamond, where the NV center only sees noise from ^{1}H spins in the oil (schematic on the top right shows oil (blue), diamond (gray) and NV center (red)). The red curve corresponds to the case of a diamond coated with a 2 nm-thick Al_2O_3 layer. In this case, the NV center sees fields from both ^{27}Al and ^{1}H spins (schematic on the bottom right shows the same as on the top, but with a Al_2O_3 layer (brown) between the oil and the diamond). The analytical simulations are based on a model taken from Ref. ([11](#)) that has been generalized for multiple layers $B_{RMS}^2 = \Sigma_k \frac{5\pi}{96} \rho_k \left(\frac{\mu_0 \hbar \gamma_k}{4\pi} \right)^2 \left(\frac{1}{d_k^3} - \frac{1}{(d_k+\delta_k)^3} \right)$, where ρ_k denotes the nuclear spin density, γ_k the nuclear spin gyromagnetic ration, d_k the position and δ_k the thickness of the kth layer. μ_0 denotes the vacuum permeability and $\hbar$ the reduced Planck constant.
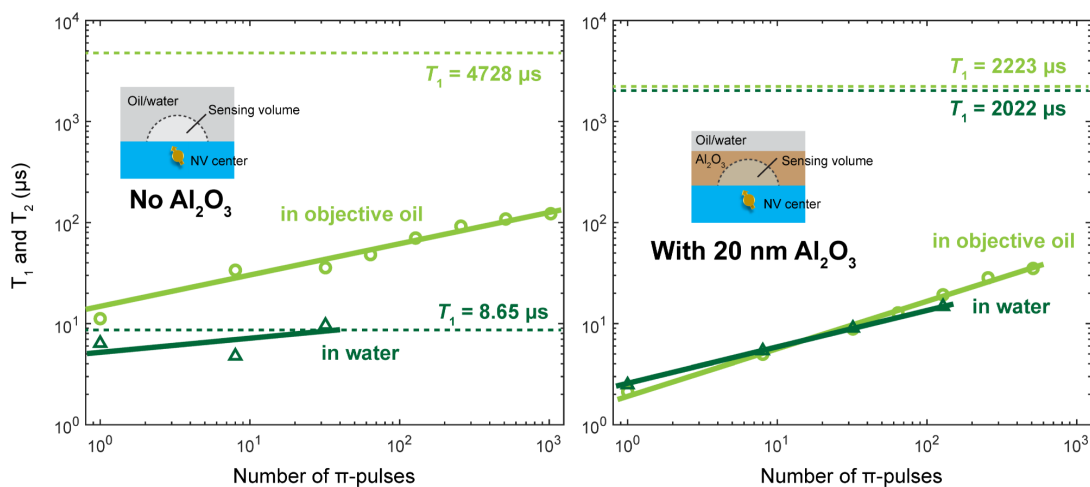
Supplementary Figure S20. Impact of a 20 nm-thick Al_2O_3 on T_1 and T_2 coherence times measured in objective oil and water **(a)** before and **(b)** after functionalization. For shallow NV centers studied here, these two environments (oil vs. water) led to clearly different T_1 and T_2. By contrast, when a 20 nm-thick Al_2O_3 layer was deposited to the diamond surface, essentially serving as a blocking material to separate shallow NV centers away from the oil/water environment, similar T_1 and T_2 were obtained as shown in (b). This further corroborates the conclusion from main text Figure *4B-D* that the Al_2O_3 layer is a cause of the observed finite but significant T_2 decrease after functionalization when imaged in oil. The effects in water will need further study. All measurements were performed at 2000 G magnetic field strength. T_2 was measured using Carr-Purcell-Meiboom-Gill (CPMG) pulses. See Supplementary Table S3 for detailed fitting parameters.
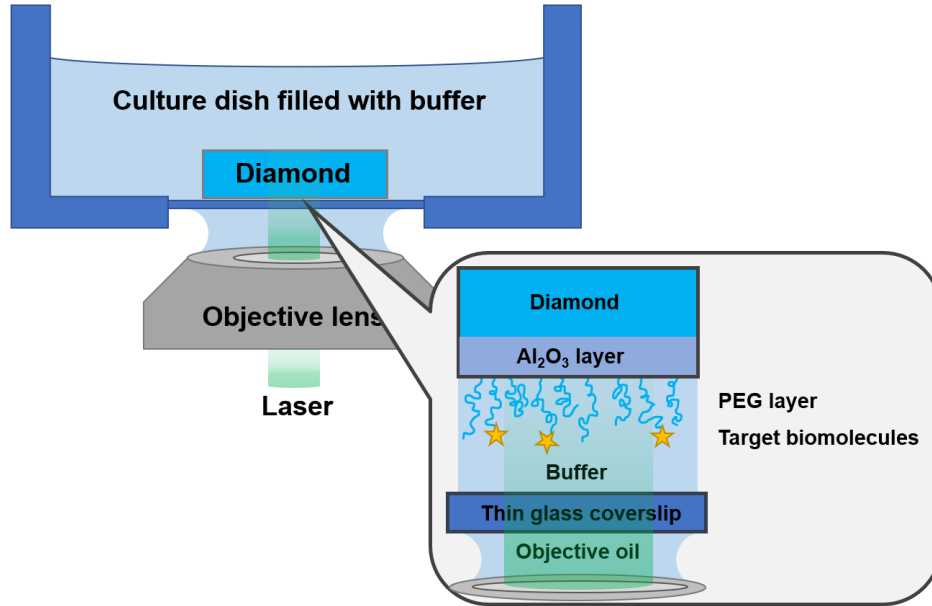
Supplementary Figure S21. Illustration of the imaging configuration. In some experiments, as indicated in each case, samples were imaged in Invitrogen SlowFade Diamond Antifade Mountant (refractive index 1.42) instead of buffer for improved sensitivity and photostability. For both single-molecule fluorescence imaging and NV confocal imaging, Olympus Type F immersion oil (n = 1.518) was used.

Captions for Supplementary Movies S1 and S2

Supplementary Movie S1. The movie shows a series of fluorescent single-molecule images (500 ms integration per frame) of Cy3-labeled ssDNA molecules immobilized on a diamond surface via biotin-streptavidin interaction. The field-of-view corresponds to a 38 × 38 µm^2 area.

Supplementary Movie S2. The movie shows a series of fluorescent single-molecule images (500 ms integration per frame) of Cy3-labeled ssDNA molecules immobilized on a diamond surface via SPAAC interaction. The field-of-view corresponds to a 38 × 38 µm^2 area.

SI References

1.   R. Champaneria, P. Mack, R. White, J. Wolstenholme, Non-destructive analysis of ultrathin dielectric films. *Surf. Interface Anal.* **35**, 1028-1033 (2003).
2.   T. Drobek, N. D. Spencer, Nanotribology of surface-grafted PEG layers in an aqueous environment. *Langmuir* **24**, 1484-1488 (2008).
3.   F. Oesterhelt, M. Rief, H. E. Gaub, Single molecule force spectroscopy by AFM indicates helical structure of poly(ethylene-glycol) in water. *New J. Phys.* **1**, 6 (1999).
4.   S. Pasche, J. Vörös, H. J. Griesser, N. D. Spencer, M. Textor, Effects of ionic strength and surface charge on protein adsorption at PEGylated surfaces. *J. Phys. Chem. B* **109**, 17545-17552 (2005).
5.   N. Ziębacz, S. A. Wieczorek, T. Kalwarczyk, M. Fiałkowski, R. Hołyst, Crossover regime for the diffusion of nanoparticles in polyethylene glycol solutions: influence of the depletion layer. *Soft Matter* **7**, 7181-7186 (2011).
6.   O. Keller, *Principles of nano-optics principles of nano-optics*, Lukas Novotny and Bert Hecht , Cambridge U. Press, New York, 2006. (2007).
7.   Z. Shu *et al.*, Unambiguous nuclear spin detection using an engineered quantum sensing sequence. *Phys. Rev. A* **96**, 051402 (2017).
8.   B. L. Dwyer *et al.*, Probing spin dynamics on diamond surfaces using a single quantum sensor. *arXiv: 2103.12757* (2021).
9.   B. A. Myers, A. Ariyaratne, A. C. B. Jayich, Double-quantum spin-relaxation limits to coherence of near-surface nitrogen-vacancy centers. *Phys. Rev. Lett.* **118**, 197201 (2017).
10.   Y. Romach *et al.*, Spectroscopy of surface-induced noise using shallow spins in diamond. *Phys. Rev. Lett.* **114** (2015).
11.   L. M. Pham *et al.*, NMR technique for determining the depth of shallow nitrogen-vacancy centers in diamond. *Phys. Rev. B.* **93** (2016).